Mon. Not. R. Astron. Soc. **000**, 000–000 (0000) Printed 27 January 2000 (MN LaTeX style file v1.4)

Stokes imaging of the accretion region in Magnetic Cataclysmic Variables – II. V347 Pav.

S. B. Potter,[1⋆] Mark Cropper,[1] and P. J. Hakala[1,2]

[1] *Mullard Space Science Laboratory, University College London, Holmbury St. Mary, Dorking, Surrey RH5 6NT*
[2] *Observatory and Astrophysics Laboratory, FIN-00014, University of Helsinki, Finland*

ABSTRACT

In this paper we present an objective map of the cyclotron emission region in a magnetic Cataclysmic Variable from polarimetric observations of the AM Her system V347 Pav. As the system parameters of V347 Pav (for example its inclination) have not been well determined, we describe an extension to Stokes imaging of Paper 1 which also searches the system parameter space.

We show that the cyclotron emission from V347 Pav emanates from two areas on the white dwarf, one area consisting of two relatively large regions located at opposite footprints of the same field lines and a much smaller region located above the orbital plane on the opposite face of the white dwarf. This is different from previous less objective techniques in which two long thin arc-shaped cyclotron emission regions were used to model the observed polarimetric variations.

Key words: accretion, accretion discs – methods: analytical – techniques: polarimetric – binaries: close – novae, cataclysmic variables – X–rays: stars.

1 INTRODUCTION

V347 Pav (RE J1844-741) was discovered during the first all–sky survey in the extreme–UV (EUV) region of the spectrum by the Wide Field Camera (WFC) on board the *ROSAT* satellite (Wells et al. 1990). Follow–up optical observations by O'Donoghue et al. (1993) showed a high EUV–to–optical ratio and substantial variations in the cycle–to–cycle light curve on a suggested 90–min period. They also obtained time-resolved spectroscopy which showed a clear 90–min period, in approximate agreement with the photometric data.

Bailey et al. (1995) obtained phase–dependent spectropolarimetric data of V347 Pav. These spectra showed strong positive circular polarization with a spectral energy distribution rising towards the red during the bright phase. This indicated that the system is an AM Her system (see Cropper 1990 for a review on AM Her systems). There were no resolvable cyclotron harmonic structures or Zeeman lines present in the data, making a precise magnetic field determination impossible. However, Bailey et al. (1995) pointed out, that by comparison with other AM Her systems, the rise of the spectral energy distribution towards the red, indicates that the field strength is likely to be $\lesssim$ 25MG. They also obtained phase–dependent photometry and polarimetry in several wave-bands. The circular polarization varies from positive to negative and rises from 12 per cent in the 3400-4800Å and 15 percent in the 3400–5300Å band, up to 30 per cent in the 4900–5700Å , 5500–8400Å and 6500–8400Å bands. Therefore, they suggested that V347 Pav is a 'two pole' system where the two opposite circular polarizations arise from two separate regions of opposite field polarity on the white dwarf surface. The reversal in sign of the circular polarization was not so clearly seen in the spectropolarimetric data. Bailey et al. (1995) suggested that this indicates that the pole producing the positive polarization is the dominant pole and therefore accretes more strongly. Interestingly, the circular polarization crosses through zero ~ 0.15 of a phase later in the two bluest bands compared to that in the red bands.

In parallel to these observations, Ramsay et al. (1996) also obtained polarimetric observations, which included linear polarimetry for the first time and led to somewhat different conclusions to those reached by Bailey et al. (1995). These observations were analysed using the techniques available at the time. The excellent quality of the observations make them ideal candidates for applying Stokes imaging described in Paper 1 (Potter et al. 1998). We perform this analysis here. This permits us both to determine the structure of the accretion region without pre-suppositions as to

⋆ Current address: South African Astronomical Observatory, PO Box 9, Observatory 7935, Cape Town, South Africa

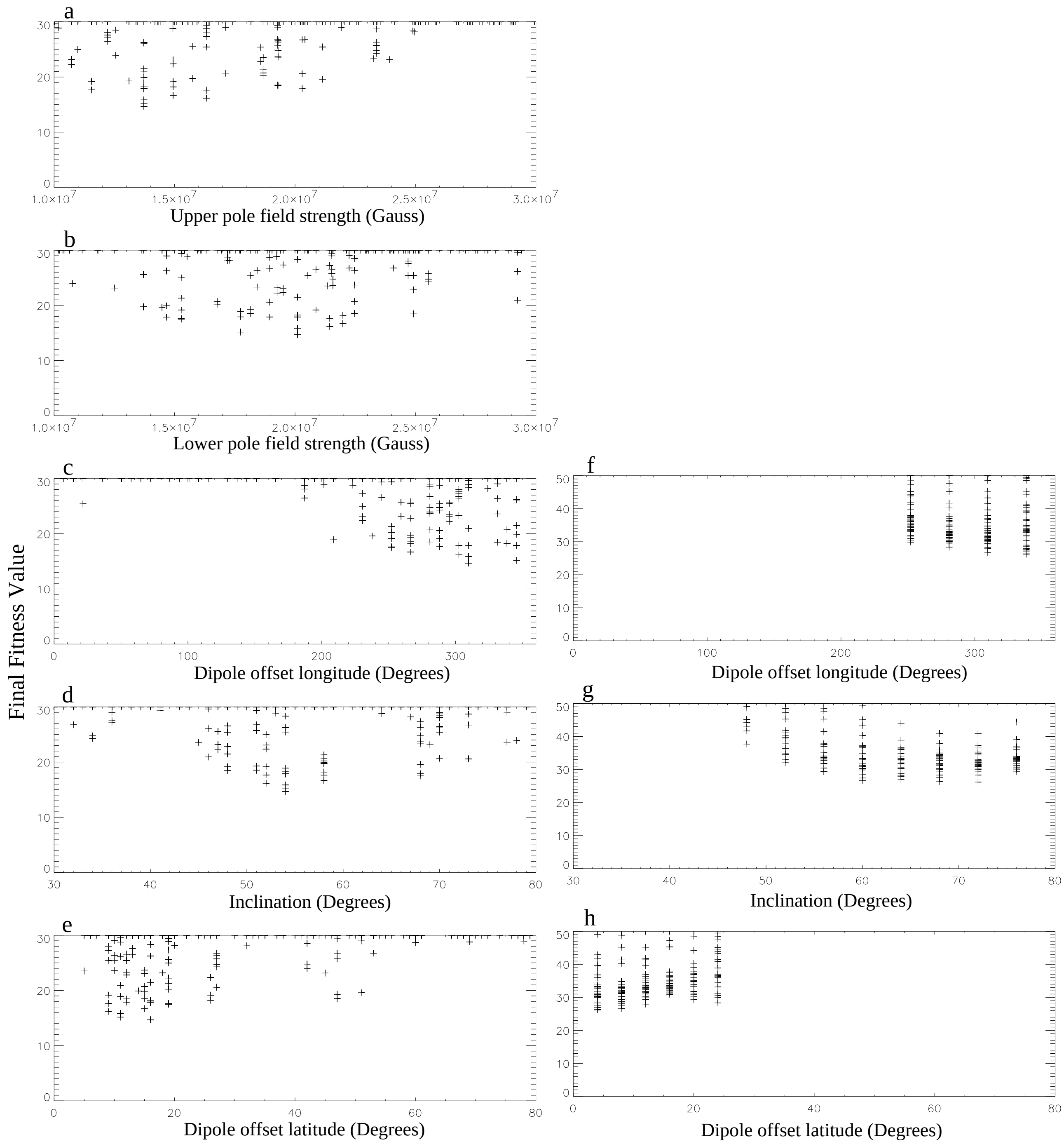

Figure 1. a-e The fitness values for the system parameters shown after genetic optimisation. **f-h** The final fitness values for the system parameters shown after a systematic search of the parameter space.

its shape and also to compare the derived structures directly with those inferred in the earlier analyses.

2 GENETICALLY OPTIMISED STOKES IMAGING

Paper 1 described Stokes imaging which models the polarized emission to map the cyclotron emission region in AM Her stars in a maximally objective manner. There it was explained that the system parameters were not included in the optimisation procedure, because these parameters are qualitatively different from those describing each point on the derived map. Therefore, the system parameter space has to be searched separately from that searched during Stokes imaging, either by trial and error, or as we now describe, by the use of a further genetic algorithm (see Paper 1 and references therein) operating as an outer loop to Stokes imaging. There is no regularisation functional or entropy term operating on the system parameters as in Stokes imaging. Instead, the outer optimisation loop optimises the final fitness values (see Paper 1) produced by several optimised solutions. In effect, the optimised solutions produced by several runs of Stokes imaging become solutions for genetic optimisation themselves. The procedure can be summarised in the following steps: Generate an initial set of random solutions for the system parameters; calculate the final fitness value for each solution using Stokes imaging and rank the solutions in order of their fitness; generate the next generation of solutions while applying mutation and cloning operators; repeat until the fitness does not improve any further.

There are five parameters to be searched in the outer loop. These are the inclination i, magnetic dipole offsets (latitudinal β and azimuthal β_ϕ) and the magnetic field strengths at each pole. The model assumes a centered dipole; however it allows the field strength at each pole to be set separately as a first order approximation for an off-centered dipole.

The procedure uses at its core cyclotron models such as the constant temperature calculations of Wickramasinghe & Meggitt (1985). Previously, fits to the polarisation data such as those of Potter et. al. (1997) have used constant temperature cyclotron models calculated for a single temperature, such as 10keV (Potter et. al. 1997). However, Potter (1999) found that a single temperature grid could not simultaneously predict the correct cyclotron spectral features in the IR at the same time as a sufficient amount of cyclotron emission in the optical wavebands in order to model the white light polarimetric variations of the AM Her system ST LMi. A combined 20keV and 5keV temperature grid gave a better model fit to the optical polarimetry and also reproduced the IR spectral features. During our initial study (Potter et al. 1998) of the data presented here in Figure 3, a constant shock temperature grid of 10keV was used. Using the 10keV grid it was difficult to obtain good model fits to the blue and red band polarimetric observations simultaneously. We therefore used the combined 20keV and 5keV temperature grid during optimisation and we find it is possible to obtain excellent fits to both wavebands simultaneously. Such a combination of models is clearly an approximation to the more complex situation involving radiative transfer through a multitemperature plasma, but we have adopted this approach as an easily implemented improvement to the single temperature models.

The size of the population for genetic optimisation was chosen to ensure a global search of the system parameter space is undertaken. The cloning and mutation probabilities were adjusted to ensure the most efficient method for searching the parameter space (Paper 1). These genetic operators are generally obtained by a trial and error approach and in the development of Stokes imaging (Paper 1) this was a relatively straightforward task. This was because one optimisation run would take a relatively short time to complete. Therefore it was possible to execute many trial solutions with different genetic operators until the most efficient and reliable values were found. However, in the case of the outer loop optimisation procedure described above, a single member of the population takes several orders of magnitude longer for its final fitness value to be computed. Given these constraints and based on our experience with Stokes imaging, we have chosen a population of 20 and a mutation probability of 0.05 to inject one mutation per generation. The cloning probability was set to zero.

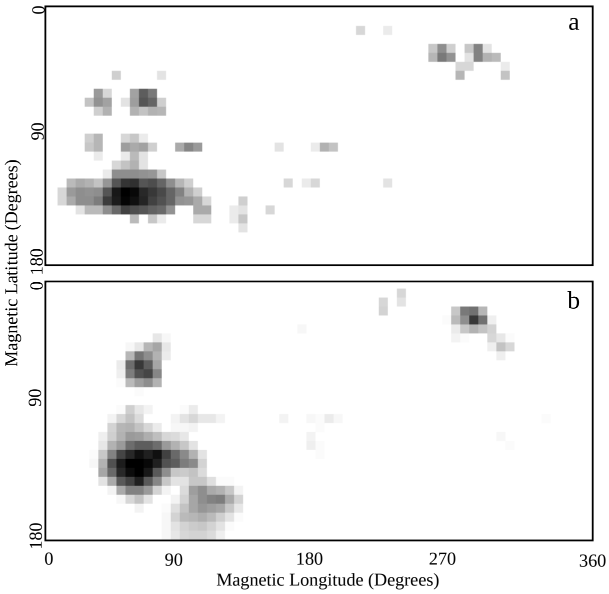

Figure 2. a The mean image map of the best solutions that have less than 5 percent of their model points at more than 5σ from the observations. See text. **b** The map of the formal best solution. (Both images are in magnetic coordinates.)

3 OPTIMISED SOLUTIONS

Ramsay et al. (1996) and Bailey et al. (1995) made their model predictions for the data to the different wavebands separately. Here we use the Stokes imaging technique to model the red and blue waveband data simultaneously: the system parameters and the location and shape of the accretion region(s) are required to be consistent in both wavebands.

After some time, the rate at which the Genetically Opimised Stokes imaging finds better solutions decreases. As explained in Paper 1, this is because the GA becomes less efficient when nearing the global minimum. The GA would eventually find the best solution, however the computation time required to do so is too large. Although the GA is not very effective at finding the best solution, it is very effective at eliminating areas of parameter space where good solutions cannot be found. The GA is therefore stopped when the rate at which better solutions are found reaches a certain threshold. We then examine the system parameters of the population of best solutions found by the GA. By doing this we deliniate the parameter space occupied by the best solutions. This parameter space is now sufficiently small to allow a systematic search.

Figures 1a to e show the values of the best optimised solutions found by the GA with final fitness values less than 20 for the 5 system parameters described above. From Figure 1a and b it can be seen that the magnetic field strengths at the two poles are not very well constrained. However, they do show broad minima centered at around 15 and 20 MG

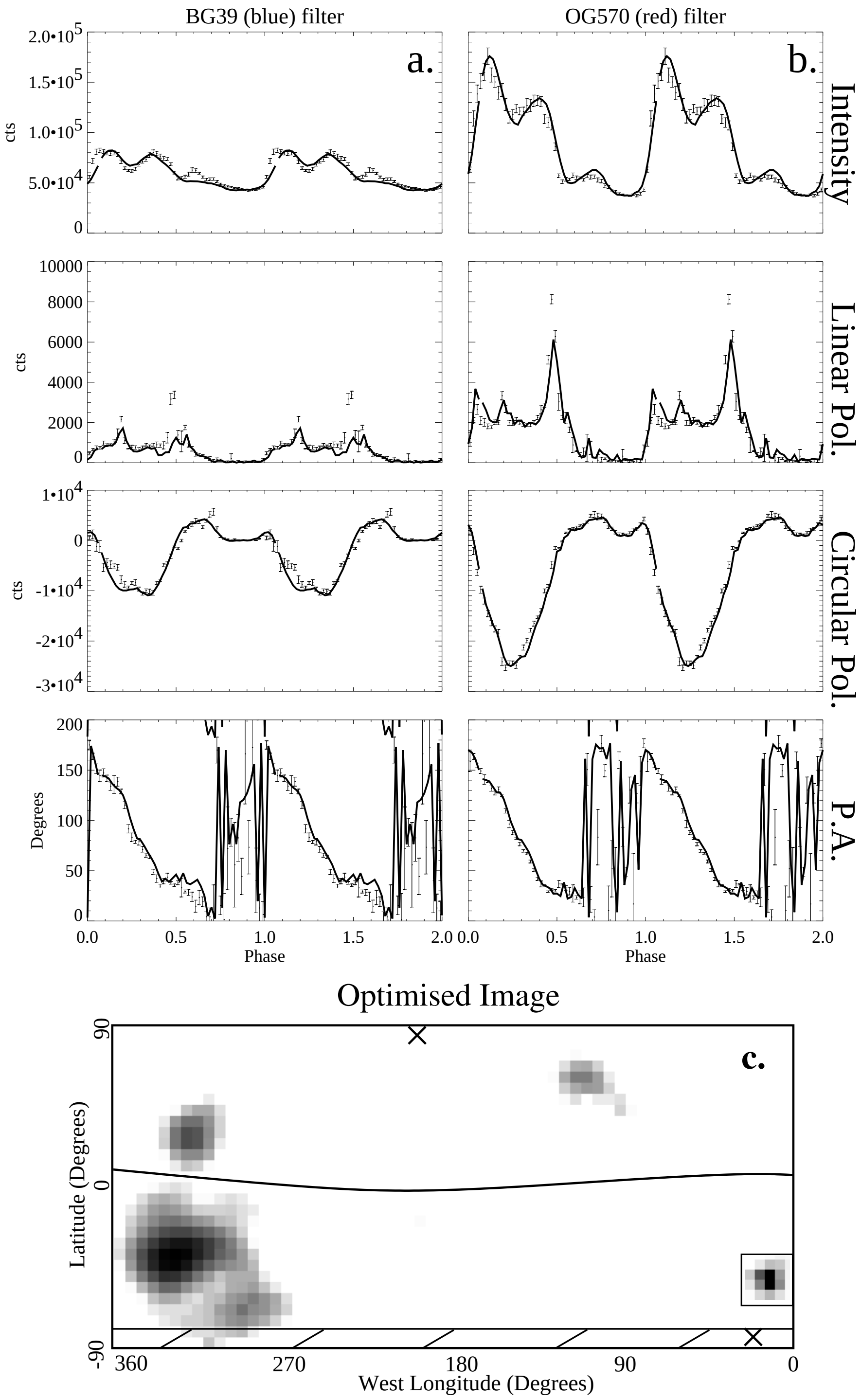

Figure 3. The Stokes imaging optimised solution to the polarimetric observations of Ramsay et al. (1996). Inclination = 68°, dipole offsets $\beta = 4^o, \beta_\phi = 338^o$. **a.** The blue data. **b.** The red data. **c.** The optimised image. Western longitudes run ahead of the line of centers of the two stars. Longitude is arbitrary because the position of the secondary is unknown. Crosses mark the location of the magnetic poles and the solid curve marks the magnetic equator. Diagonal strips indicate the area of the white dwarf surface that is permanently self occulted from Earth. The spot within the box represents the resolution of the image (see text).

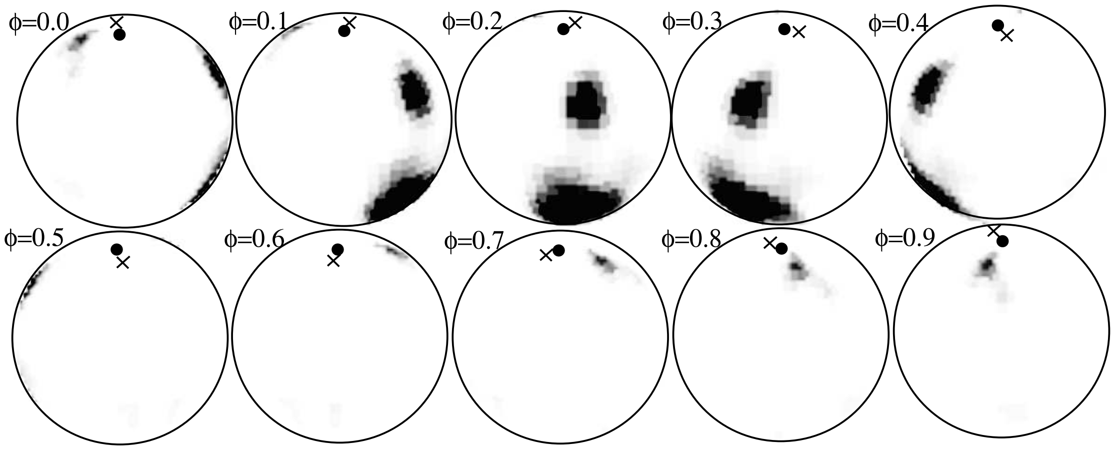

Figure 4. The position of the cyclotron emission regions as viewed from Earth for a complete orbital rotation. The dot and the cross represent the spin and magnetic poles respectively.

for the upper and lower poles respectively. We are modelling broad band polarimetric observations in which an accurate estimate for the magnetic field strength is not required. We therefore adopt these values for the magnetic field strengths which are also in approximate agreement with those estimated by Bailey et al. (1995) from their spectropolarimetric observations.

Figures 1c,d and e show the best optimised solutions found by the GA for the angles describing the phase at which the upper magnetic pole crosses our line of sight β_ϕ, the inclination (i) and the magnetic dipole offset from the spin axis (β). These angles show more defined minima than the magnetic field strengths, allowing a more systematic search to be carried out. We therefore searched i between $48-76^o$ and β between $4-24^o$ in steps of 4^o and β_ϕ between $252-338^o$ in steps of $\approx 30^o$.

The results of the systematic search are shown in Figures 1f,g and h. The relative minimum values between the systematic search and the genetic search are different because a larger value for the Lagrangian Multiplier (paper 1) was used in the systematic grid in order to find smoother image solutions. The formal best solution has an inclination of 68^o and magnetic dipole offset angles of $\beta = 4^o$ and $\beta_\phi = 338^o$. Figures 1f,g and h however, suggests that there are several solutions with similar final fitness values. We therefore examined each of the model fits to the polarimetric data in turn. For each model fit we created a distribution of residuals (in terms of data uncertainty) between every data and model point (there are 400 data points). We then rejected solutions that have more than 5 percent of their model points at more than 5σ from the observations. The solutions that remain are found with system parameter values in the range $64^o < i < 72^o$, $0^o < \beta < 8^o$ and $310^o < \beta_\phi < 340$. The formal best solution is of course within this parameter range. For comparison, solutions that have less than 7.5 percent of their model points at more than 5σ from the observations are found with system parameter values in the range $60^o < i < 76^o$, $0^o < \beta < 16^o$ and $280^o < \beta_\phi < 340$.

The model solutions within the 5 percent criteria all provide excellent fits to the polarisation data and their image solutions for the location and structure of the emission regions all appear to be similar. Figure 2a shows the mean image created from all the image solutions within this parameter range. The mean image includes the formal best solution (Fig 2b) which we now use to continue the discussion.

4 OPTIMISED MODEL FIT

The formal best solution is shown in Figure 3. The optimised model solution has reproduced the red polarization data remarkably well. The gross morphology of all the red polarized light curves has been accurately predicted and in particular, the variation in position angle, the relative amounts of linear and circular flux, the peaks and dips in the circular polarization and the overall variation in the intensity curve.

The model fit to the blue polarimetric observations (Figure 3a) has similarly been reproduced well, but closer inspection of the blue model prediction shows that it has underestimated the blue linearly polarized pulse at $\phi \sim 0.5$. This may have arisen because of an insufficiently accurate determination for the magnetic field strengths. The red polarimetric observations have significantly more counts and lower uncertainties than the blue band, so the optimisation routine will be more biased towards fitting the red data. The blue linear pulse exists in the observational data only as two data points, so a poor fit to these points will have an insignificant effect on the overall fitness value. We are currently investigating improvements to the technique (such as calculating the goodness of fit to the change in the slope of the data, Garcia 1998) which will be the subject of a future paper.

The Stokes imaging has predicted that the bright phase emission emanates from a large region towards the lower hemisphere and the faint phase emission from a single smaller region in the upper hemisphere of the white dwarf (Figure 3c). The main emission region appears to consist of two regions located at opposite footprints of the same field lines. The secondary emission region in the upper hemisphere is relatively less dense than the main emission region. It is also much smaller in size and almost diametrically opposed to the main emission region.

In Paper 1 it was explained that reproducing the shape and structure of the emission region is an under constrained problem so it was necessary to include a smoothness (regularisation) term in the fitting process. To investigate the effect of this regularisation term we created an artificial emission spot and placed it at the same location as the center of the main emission region. We then applied the optimisation technique to the artificial polarized light curves that the spot would produce in an attempt to recover the original image. The resulting image is shown towards the bottom right hand corner of Figure 3.c. This gives an indication of the resolution of the reconstructed image and suggests that some of the broadness of the main emission region can be attributed to the technique.

Figure 4 shows the emission regions mapped onto a sphere representing the surface of the white dwarf as viewed from Earth for a complete orbital rotation. The observed features of the polarimetric observations (Figure 3a,b) can be explained with reference to this figure. The most prominent feature of the observations is the bright and faint phase. The two main emission regions are responsible for the bright phase emission during $\phi \sim 0.0$–0.5 and the secondary smaller emission region is responsible for the faint phase emission during $\phi \sim 0.5$–1.0. The slightly diagonal orientation of the lower main emission region (seen more clearly in Figure 3c) means that it disappears over the limb of the white dwarf at $\phi \sim 0.5$–0.6 slightly more rapidly than it appears over the limb of the white dwarf at $\phi \sim 0.0$ resulting in a larger linearly polarized pulse at the end of the bright phase. This main emission region remains on the limb of the white dwarf resulting in enhanced linear flux throughout the bright phase (enhanced linear flux is seen when the emission region is viewed close to 90° to the magnetic field lines that feed it). The large amounts of negative circularly polarised flux seen during the bright phase results from the summed emission from the two larger emission regions, the upper emission region producing positive circular flux.

The secondary emission region first appears over the limb of the white dwarf at $\phi \sim 0.5$–0.6 and therefore also contributes to the large linearly polarized pulse. At $\phi \sim 0.8$ the magnetic field lines feeding the secondary emission region are most pointing towards the line of sight resulting in depolarization of the radiation by cyclotron self–absorption as observed by the dip in the positive circular polarization. The secondary region then moves away from the line of sight, resulting in an increase in emission (seen as the contribution to the rapid increase in the intensity) and the brief increase in positive circular polarization at $\phi \sim 0.8$–1.0 until the main emission region dominates at $\phi \sim 1.0$. The more gradual decline in the intensity from the bright phase at $\phi \sim 0.5$ (seen especially in IR observations in Bailey et al. 1995) can be attributed to the presence of the secondary region. At $\phi \sim 0.2$ the secondary region disappears over the limb of the white dwarf resulting in the linear pulse seen in both red and blue bands.

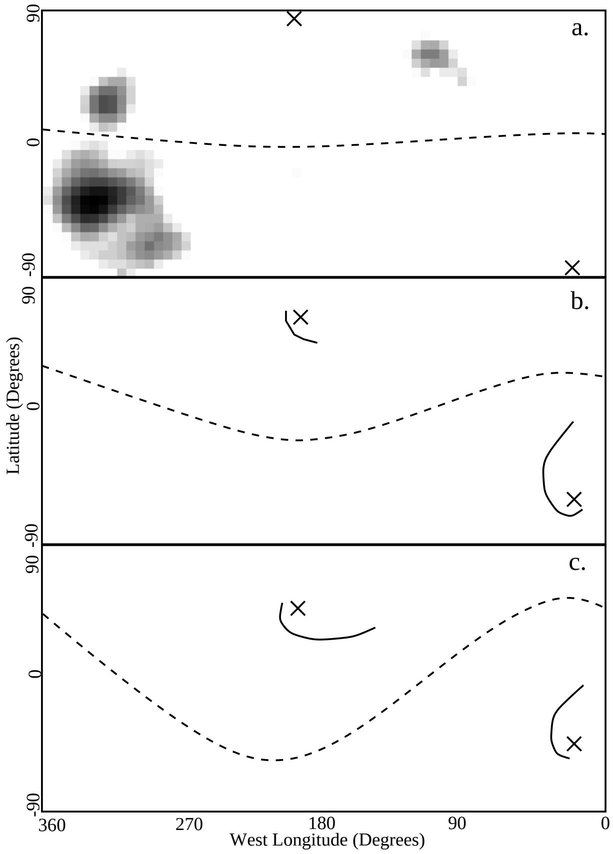

Figure 5. A comparison between: **a.** The optimised image solution. **b.** The model prediction in Ramsay et al. (1996) **c.** The model prediction of Bailey et al. (1995). All are in white dwarf spin coordinates. Crosses mark the location of the magnetic poles. **Dashed** curve marks the magnetic equator.

5 DISCUSSION

5.1 The accretion region

In Figure 5 we compare the prediction for the shape and location of the cyclotron emission region with those of previous work. The figures are mapped onto a flat surface. As a result, the large differences in longitude near the polar regions are much smaller on the surface of a sphere. The emission regions are mapped onto the same white dwarf spin coordinate system in each case. However, the alignment in longitude between each image is unknown. **Nevertheless, one would expect the emission regions to be roughly aligned at the same longitude in all cases in order to get the maxima and minima in the light curves. In Figure 5 we align and compare each image with respect to their magnetic poles.** Figure 5a is our best solution.

Figure 5b shows the prediction for the shape and location of the emission region from Ramsay et al. (1996). The main difference between Figures 5a and 5b is that Ramsay et al. (1996) located the narrow arc–like main emission region, responsible for the negative polarization, on the upper hemisphere of the white dwarf. They also used a much higher value for the inclination (80°) as an explanation for the equal orbital coverage of the bright and faint phases and the variation in the position angle.

Figure 5c shows the model prediction of Bailey et al. (1995) mapped onto the same coordinate system as Figures 5a and b. They predict two long thin arcs located in approximately the same locations as that of Ramsay et al. (1996). However, they locate the main emission region in the lower hemisphere in agreement with Stokes imaging. Furthermore, Bailey et al. (1995) estimated an orbital inclination of $i = 60^{\circ}$ similar to that found here but a larger magnetic dipole offset of $\beta = 50^{\circ}$.

In all three cases the emission region is seen to extend over a large range in magnetic latitude. In figures 5b and c the main emission arcs are seen to extend to magnetic latitudes of $\sim 45^{\circ}$. The optimised solution also predicts the main bulk of the emission at $\sim 45^{\circ}$ and trailing off towards the magnetic equator. As discused ealier, some of the extension in the optimised image can be attributed to the regularisation term of the technique.

5.2 The cyclotron emission

The genetically optimised Stokes imaging technique predicts different magnetic field strengths for the upper and lower magnetic poles. Furthermore, the different locations of the emission regions means that material has free-fallen from different heights resulting in slightly different shock temperatures. If this is the case, the peak in the cyclotron flux from the different emission regions ought to occur at different wavelengths. This prediction can explain the simultaneous negative circular polarization in the red bands and the positive circular polarization in the blue bands at phase ~ 0.4 of the Bailey et al, (1995) observations. On our ephemeris (Ramsay et al. 1995) this translates to $\phi \sim 0.9 - 1.0$. At $\phi \sim 0.8$–1.0 the model predicts both emission regions to be in view simultaneously. Therefore, the positive circular polarization from the secondary emission region dominates in the blue at $\phi \sim 0.9$ while the negative circular polarization from the main emission region dominates in the red. During $\phi \sim 0.9$–1.0, the secondary emission region begins to disappear while more of the main emission region begins to appear and dominates the circular polarization at all wavelengths.

5.3 The threading region

The structure of the accretion region in AM Her stars depends on how and where the accreting material attaches to the field lines at the threading region. A number of physical processes and instabilities are competing in the region making a theoretical study difficult (see Warner 95 and references therein). The map produced for the emission region of V347 Pav can give some indication of where and how material threads on to the magnetic field lines in V347 Pav.

From Figure 3c and 4 it can be seen that most of the accreting material reached the surface of the white dwarf in the lower hemisphere. The main emission region extends from close to the magnetic pole to almost the magnetic equator with the bulk emission occuring at approximately 45° in magnetic latitude. This means that material leaving the Inner Lagrangian point must have attached to magnetic field lines over a spread in azimuth at the threading region. one explanation for this could be Kelvin-Helmholtz instabilities striping material from the surface of the main flow close to the Inner Lagrangian point with the result that some material accretes close to the magnetic pole. The main bulk of material then survives longer and penetrates deeper into the magnetosphere before becoming threaded and giving rise to the main bulk of emission. Some unthreaded larger blobs may then penetrate further before becoming threaded. Some material also followed the same field lines onto the white dwarf above the orbital plane. With such a low dipole offset angle ($\beta = 4^{\circ}$) it is not too difficult to envisage how material can go either (or both) way down the magnetic field lines.

The secondary smaller emission region is located closer to the magnetic pole. As a result the material which attached to the field lines that feed this region did so much closer to the Inner Lagrangian (L1) point. This again implies that some material is somehow stripped from the main bulk flow of material before the magnetic pressure overcomes the main flow.

This also has implications for the possible location of the secondary star in the orbital plane. With the use of Figure 4 one can see that were the secondary star to feed the secondary emission region first then the secondary star is most likely to cross our line of sight at $\phi \sim 0.9$–0.2: any earlier or later in phase would result in accretion onto the main emission regions. By this time the accreting material has penetrated quite deep into the magnetosphere of the white dwarf making it improbable for material to attach to field lines that would feed the secondary emission region. However, our knowledge of the trajectories of the accretion stream in these systems is still too inadequate to make a definitive statement.

5.4 The system parameters

We have shown that it is possible to obtain good fits to the polarimetric data within a range of the system parameter space. Indeed some of the rejected fits are much better than those obtained by previous less objective techniques. The derived value for the dipole offset β is small and consistent with zero. This is the lowest energy configuration for a synchronised system (eg. Campbell 1997), but until now the derived offsets in AM Hers have been determined to be randomly orientated (eg Brainerd & Lamb 1985) and generally non-zero.

We note that the principle method for obtaining the system parameters in AM Her type systems is from polarimetric observations. However we have found from this investigation that even with the highest quality polarimetric data and the most objective technique for modelling the cyclotron emission so far, the derived parameters are very different from those which would have been derived assuming radial accretion near the magnetic pole. Moreover, because of freedom to orientate the dipole relative to the spin axis, the acceptable range for the system parameters can be quite large. This has severe implications for the accuracy of previous estimates of AM Hers as a whole.

6 SUMMARY

In this paper we have applied an extension of the Stokes imaging technique, developed and discussed in Paper 1, simultaneously to the blue (3500–6500Å) and red (5500–9500Å) polarimetric observations of the AM Her star V347 Pav from Ramsay et al. (1996). We also describe an extension to the Stokes imaging technique, which in addition searches the system parameter space.

The technique has predicted an extended main cyclotron emission region, located in the lower hemisphere of the white dwarf, and a secondary, smaller less dense region almost diametrically opposite. The main emission region is found to consist of two relatively higher density regions centered on the magnetic equator. It is slightly behind and trailing the lower magnetic pole in phase. These maps are qualitatively different from those previously derived using less objective techniques in which two long thin arcs were used in an attempt to reproduce the polarimetric variations.

The formal best fit to the observations were obtained for a system inclination of $i = 68^o$, a magnetic dipole offset angle of 4^o, and magnetic field strengths of 15 and 20 MG for the upper and lower poles respectively. These fits were obtained when the upper magnetic dipole crosses the line of sight to the observer at phase ~ 0.06. Solutions which have lower than 5 percent of their model points at more than 5σ from the observations have system parameter values in the range $64^o < i < 72^o$, $0^o < \beta < 8^o$ and $310^o < \beta_\phi < 340$. Maps within this range were all found to be very similar to that from the formal best solution. **Based on these results we note that this technique cannot constrain the system parameter space too well.**

The accuracy in the determination of the magnetic field strengths are less certain with good fits possible within the range 10–30 MG. However, better fits are obtained when the upper magnetic pole has a magnetic field strength of ~ 5 MG, lower than the lower pole. We have also shown that the simultaneous appearance of both emission regions at $\phi \sim 0.8$–1.0 in the model, can explain the simultaneous observed positive circular polarization in the red wave–bands and the negative circular polarization in the blue wave–bands in the multi-wave band observations of Bailey et al (1995).

We have presented a simple view of the threading process in this system. The main bulk of the accretion flow penetrates quite deep into the magnetosphere of the white dwarf forming the main accretion region relatively close to the magnetic equator. However we suggest some material attaches to magnetic field lines much closer to the L_1 point resulting in a secondary much smaller accretion region closer to the magnetic pole on the upper hemisphere of the white dwarf. Finally, using some simplified arguments we predict the secondary star to cross our line of sight at $\phi \sim 0.9$–0.2.

7 ACKNOWLEDGMENTS

SBP acknowledges the PPARC for financial support in the form of a research studentship. PJH is supported by an Academy of Finland research fellowship.

REFERENCES

Bailey, J. A. et al., 1995, MNRAS, 272, 579.
Brainerd, J. J. & Lamb, D. Q., 1985, Proceedings of the Seventh North American Workshop, (A85-48276 23-90). Dordrecht, D. Reidel Publishing Co., , p. 247-256
Campbell, C. G., 1997, Magnetohydrodynamics in Binary Stars, Kluwer Academic Publishers.
Cropper, M. S., 1990, MNRAS, 231, 597.
O'Donoghue, D., et al., 1993, MNRAS, 265, 545.
Garcia, G., 1998, MSc thesis, University College London.
Potter, S. B., Cropper, M. S., Mason, K. O., Hough, J. H., Bailey, J. A., 1997, MNRAS, 285, 82.
Potter, S. B., Hakala, P. J. & Cropper, M, (Paper 1) 1998, MNRAS, 297, 1261.
Potter, S. B., Hakala, P. J. & Cropper, M, 1998, Annapolis Workshop on Magnetic Cataclysmic Variables, ASPCS, Vol. 157.
Potter, S. B., 1999 MNRAS, submitted.
Ramsay, Gavin., Cropper, M., Wu, K. & Potter, S., 1996, MNRAS, 282, 726.
Warner, B. 1995, Cataclysmic Variable Stars, Cambridge Astrophysics Series 28, Cambridge University Press.
Wells, A. A. et al., 1990, Proc. SPIE, 1344, 230.
Wickramasinghe, D. T. & Meggitt, S. M. A., 1985 , MNRAS, 214, 605.